Nuclear Instruments and Methods in Physics Research A 1084 (2026) 171254

Contents lists available at ScienceDirect

Nuclear Inst. and Methods in Physics Research, A

journal homepage: www.elsevier.com/locate/nima

Full Length Article

Proton microbeam studies of charge collection efficiency in large area silicon carbide detectors

A. Spatafora [a,*], D. Carbone [a], L. La Fauci [a], G.A. Brischetto [a], D. Calvo [b], F. Cappuzzello [a,d], M. Cavallaro [a], A. Crnjac [c], K. Ivanković Nizić [c], M. Jakšić [c], D. Torresi [a], S. Tudisco [a], for the NUMEN collaboration

[a] INFN-Laboratori Nazionali del Sud, Catania, Italy
[b] INFN-Sezione di Torino, Torino, Italy
[c] Ruder Bošković Institute, Division of Experimental Physics, Zagreb, Croatia
[d] Dipartimento di Fisica e Astronomia "Ettore Maiorana", Università di Catania, Catania, Italy

ARTICLE INFO

Keywords:
SiC detectors
IBIC
Charge collection efficiency
Particle detectors

ABSTRACT

Large area, p–n junction, silicon carbide (SiC) detectors will be used to construct the new particle identification system of the focal plane detector of the MAGNEX magnetic spectrometer foreseeing the NUMEN experimental campaigns. The present work aims to the characterization of these devices in terms of the charge collection efficiency (CCE) both in the inner areas and along the perimeter. Ion beam induced charge technique with a proton microprobe is used for obtaining a 3D characterization of the CCE of the SiC detectors. The technique allows to draw the CCE profile with accuracy as low as 10 μm along the surface area and to explore a possible dependence on the depth of the detectors by exploring a range of proton incident energies from 1.26 to 3.92 MeV. In the inner area a good uniformity in the signal collection is found, whereas an anomalous behavior is observed in two of the four edges. The present results suggest the necessity to improve the wafer cutting techniques together with a recast of the edge structures.

1. Introduction

Thanks to their high radiation hardness and high energy and time resolution [1–8], several new generation particle detector systems are planning to use Silicon Carbide (SiC) detectors [9–13]. As an example, in the PARIDE project [10] the plan is to construct a new portable and versatile particle identification (PID) system based on SiC-Cesium Iodide (CsI) tallium doped (Tl) telescope detectors, suitable to detect heavy ions in nuclear physics reactions.

It is also the case of the NUMEN experiment [11,12], which aims to measure accurate cross section of heavy-ion induced Double Charge-Exchange (DCE) reactions, because of their link to neutrinoless double beta decay ($0\upsilon\beta\beta$) [14,15]. The DCE reactions are explored at the Laboratori Nazionali del Sud of the Istituto Nazionale di Fisica Nucleare (INFN-LNS) in Catania using the Superconducting Cyclotron to accelerate the beams, and the MAGNEX large acceptance magnetic spectrometer [16,17] to detect the reaction products. Since the DCE cross sections are quite low (tens of nb [18,19]), a major upgrade of the LNS facility was launched to increase the beam intensities up to 10^{13} pps, requiring the development of new technologies for the accelerator, the target system, as well as the detection systems coupled to the MAGNEX spectrometer [20–25]. In particular, telescopes based on thin SiC detectors and thicker CsI(Tl) inorganic scintillators were chosen as the NUMEN solution for PID. Each telescope covers an area of 15 × 15 mm^2 with a dead space of 0.4 mm between each cell, in order to maximize the geometrical efficiency. Large area SiC detectors will be used as the ΔE stage. The SiC detectors produced to this purpose are single pad, 100 μm thick epitaxial layer, 10 μm thick dead layer in the back side, 15.4 × 15.4 mm^2 area including 400 μm edge structure. A 5 mm-thick CsI(Tl) crystal is used to measure the residual energy by means of a photodiode to collect the scintillation light. To cover the large MAGNEX detection area (154 × 1260 mm^2) 720 telescopes will be used, arranged in 36 towers, each of them having 10 rows and 2 columns. A similar geometry is chosen for the PID system of the PARIDE project, which is composed by three towers only. Thus, it would be crucial to have homogeneity among different SiC devices in terms of depletion voltage, thickness, resolution, and charge collection uniformity within each detector.

The PID procedure adopted in MAGNEX is based on the combination of two techniques [26]. The needed parameters are measured by the

* Corresponding author.
E-mail address: alessandro.spatafora@lns.infn.it (A. Spatafora).

https://doi.org/10.1016/j.nima.2025.171254
Received 8 August 2025; Received in revised form 23 December 2025; Accepted 23 December 2025
Available online 31 December 2025

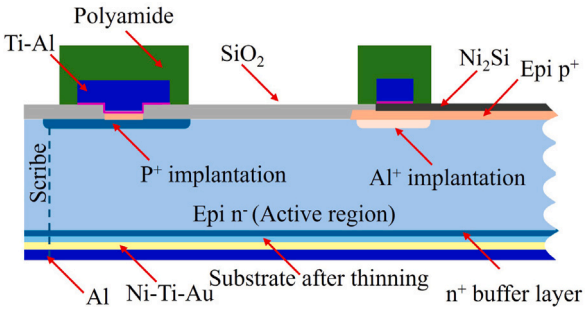

Fig. 1. Sketch of the sectional view illustrating the internal structure of the SiC device (not to scale).

focal plane detector (FPD), composed by a gas tracker [21] and the PID system of SiC-CsI(Tl) telescopes. The atomic number (Z) of the ions is identified by the standard ΔE-E technique, based on the Bethe-Bloch formula [27]. The residual energy (E_{resid}) is measured by the CsI(Tl) crystals, and the energy loss by the SiC detectors. For the mass identification (A), the correlation between the kinetic energy and the magnetic rigidity is exploited. In the experimental conditions of the NUMEN reactions, in which oxygen, fluorine and neon ions are involved, the identification procedure is successfully performed using the X_{foc}-E_{resid} correlation, in which X_{foc} is the horizontal position measured by the gas tracker detector. The relationship between the two quantities is approximately quadratic with a factor depending on the ratio $\sqrt{m}/q$. A crucial point for the NUMEN project is the capability of the PID technique in terms of the minimum cross-section significantly measurable by the MAGNEX spectrometer, since the aim is the accurate measurements of very rare processes like DCE reactions, characterized by cross sections as low as tens of nbarn. In this context, on one hand the geometrical efficiency of the PID system should be high, and on the other hand the background coming from events with partial charge collections, which could reduce the overall sensitivity, should be maintained as low as possible, in order to maximize the signal to noise ratio. Thus, uniformity in charge collection efficiency (CCE) inside the sensors active volume is a fundamental requirement to be verified for applications in nuclear physics experiments, e.g. the NUMEN project. Moreover, the knowledge of the overall detection efficiency in complex detection apparatuses, as the MAGNEX PID system, typically comes from the implementation of advanced simulation tools (e.g. GEANT4 [28,29]) requiring as an input the CCE behavior in the detector volume, especially along the edge structures.

In the last few years, we started a wide test campaign both with radioactive sources and ion beams, to fully characterize the SiC detectors. In Ref. [8] the I-V and C-V characteristics and the response of the SiC detectors under irradiation with α-source were studied. We also recently discussed a study of the energy loss for SiC material and the SiC detector depletion depth measurements [30]. In this paper we report the CCE characterization of four SiC detector prototypes performed at the Ruđer Bošković Institute Accelerator Facility (RBI-AF) in Zagreb, exploiting the ion beam induced charge (IBIC) microprobe technique [31] with proton beams. This method is widely used for measuring the charge transport properties in solid state detectors [32–36]. A 3D characterization of the SiC detector CCE is performed, testing the response along the surface of the detector with micrometer precision and also at different depths by exploring a range of proton incident energies from 1.26 to 3.92 MeV. Some areas of the detectors are irradiated, both in the inner volume and at the four edges.

The paper is organized as follows. We describe the tested SiC sensors in Section 2 and the experimental setup in Section 3. Then, the data reduction and the main results are presented in Section 4. Conclusions are drawn in Section 5.

2. Large area silicon carbide detectors

SiC detectors are nowadays a valuable alternative to Silicon (Si) detectors for applications in particle detection [7]. The main reason is the much higher resistance to high doses of particle irradiation [37] of SiC detectors with respect to Si ones. Recently, it was found that a dose as high as 10^{13} ions/cm^2 of ^{16}O ions at 25 MeV incident energy is sustainable in SiC, whereas a deterioration of the signals starting from 10^9 ions/cm^2 is observed in Si detectors [2]. Another important feature of SiC detectors is that they display a leakage current three orders of magnitude smaller than the one of Si detectors.

A few prototypes of large area SiC devices were recently constructed from two epitaxial wafers, designated as TT0012-11 and RA0089-27, as described in Ref. [8]. The choices in the production of such devices are the result of the R&D phase performed within the SiCILIA project [7], in particular regarding the edge structure layout. A section sketch of a SiC device highlighting its different layers is shown in Fig. 1. They are produced starting from 100 μm n$^-$ epi-layers grown on 350 μm 4H-SiC substrates. First, a double epitaxial layer, necessary to implement the p$^+$/n junction, is built growing a p$^+$ layer 0.3–0.5 μm thick with an Al doping concentration of the order of 10^{18}-10^{19}/cm^3 over the n$^-$ epi-layer with a N doping concentration of ≈ 10^{13}/cm^3. Then, the detector and the edge-structure areas are defined by multiple photolithography steps [7]. The edge structures are built by the implantation of Al$^+$ ions (thickness of implanted region ≈ 5 μm) at the borders of the active region to reduce the electric field and P$^+$ ions at the edge of the device creating n$^+$ region that acts as a field stop. After these two implants, the dopants are activated by a high temperature process at 1650° C. The deposition of an isolation oxide (SiO_2, thickness ≈ 0.02 μm) and the opening of the contacts with a further photolithography are then performed. The front of the device is metallized by a Nickel Silicide (Ni_2Si) deposition (thickness ≈ 100 nm) and annealed in order to form a good ohmic contact on the p$^+$ and the n$^+$ regions. A selective etch removes the unreacted Ni_2Si on the oxide and a thicker layer of Ti, and Al is deposited on the periphery of the detector for the bonding [7]. Finally, front side passivation is performed by deposition of a thick polyamide layer (≈ 8 μm) and the active area of the detector is opened by a further lithography. On the back side of the device a mechanical thinning procedure is performed to reduce the total thickness of the device to ≈ 110 μm. Since the epi-layer is 100 μm thick, this corresponds to have a dead layer of ≈ 10 μm. Then, the ohmic contact is formed by an aluminum deposition (≈ 1 μm).

The epitaxial wafers used for producing the SiC detectors characterized in this work are 6” diameter and came from the same bulk material. The main difference in the two productions is the doping concentration applied to each wafer: the TT0012-11 wafer was doped with the standard concentration of ≈ 9×10^{13} atoms/cm^3 corresponding to a full depletion voltage (FDV) of ≈ 800 V, whereas the RA0089-27 wafer was doped with ≈ 3×10^{13} atoms/cm^3 (FDV ≈ 350 V). The device (shown in Fig. 2a) features a square area of 15.4 mm sideways. The total thickness as measured using a micrometer is 110 ± 1 μm. On the front, a small pad (0.15 × 0.30 mm^2) for the wire bonding is located in the center of one side.

The edge structure, ≈ 400 μm wide running around the detector and visible in Fig. 2b, corresponds to ≈ 10% of the total area of the SiC detector. It is thus important to investigate the response of the detector at the edges to estimate the total detection efficiency. In principle, the CCE should be uniform inside the active area (plain gray area in Fig. 2b), then, when the first guard ring, defined by the Al$^+$ deposition, is crossed, we expect to measure a smaller energy due to a not measurable energy loss of the particles crossing the thick polyamide layer (green layer in Fig. 1 and black rings in Fig. 2b). A successive plateaux in the detector response is expected in the region between the Al$^+$ and the P$^+$ depositions (striped gray band between the two black rings in Fig. 2b), with a very small energy loss due to the thin SiO_2 layer (gray layer in

Table 1
Full depletion voltage (FDV) [8], depletion depth (as evaluated in Ref. [30]) at the FDV and average charge collection efficiency ⟨CCE⟩ evaluated at the FDV in the A_x, A_y, E_x, and E_y edges (as indicated in Fig. 2a) around 300 μm for the irradiated SiC sensors.

Wafer	Device	FDV (V)	Depletion depth (μm)	⟨CCE⟩ (%)			
			from Ref. [30]	A_x	A_y	E_x	E_y
TT0012-11	A41	800	99.6 ± 0.1	78.85 ± 0.02	96.77 ± 0.04	99.46 ± 0.01	84.76 ± 0.04
TT0012-11	A45	800	98.6 ± 0.1	82.15 ± 0.01	99.28 ± 0.01	98.78 ± 0.02	84.12 ± 0.04
RA0089-27	A102	240	94.4 ± 0.1	82.15 ± 0.01	99.28 ± 0.01	98.78 ± 0.02	84.12 ± 0.04
RA0089-27	A106	320	94.1 ± 0.1	81.44 ± 0.06	98.86 ± 0.03	98.94 ± 0.04	86.16 ± 0.04

Fig. 1). Crossing the second guard ring, defined by the deposition of the P^+, the CCE should drop rapidly to zero.

A first campaign of tests on these devices is reported in Ref. [8]. In general, the tested SiC sensors show a good energy resolution (≈ 0.5% FWHM with α particles at ≈ 8.7 MeV). Devices belonging to the TT0012-11 wafer displayed good C-V characteristics and doping profile. On the other hand, sensors belonging to the RA0089-27 wafer are characterized by worse performances especially in terms of the doping profile and the production yield. Also, from the analysis of energy loss measurements performed in transmission with proton beams [30], it was possible to define an empirical correction to the energy loss tables of Ziegler [38] for SiC material used in the SRIM software [39]. This result is crucial, since the detectors will be used in transmission. The correction was then applied to deduce the depletion depth of the SiC detectors at the FDV, finding that it is possible to fully deplete to ≈ 100 μm the SiC devices belonging to the TT0012-11 wafer, i.e. the ones produced with a standard doping concentration of the epitaxial layer on the substrate (see Ref. [8]).

In this work, the results concerning the CCE evaluation in the active area and at the edges of the A41 and A45 SiC sensors of the TT0012-11 wafer and A102 and A106 SiC sensors of the RA0089-27 wafer are reported. Their FDV, as obtained in Ref. [8], are listed in Table 1.

3. Experimental setup

A schematic view of the ion microprobe system and the IBIC experimental setup at the RBI-AF in Zagreb is shown in Fig. 3. The ion beam was focused to a spot size of ≈ 2 μm in a microprobe system by a multiplet of quadrupole magnets, and the ion current was reduced to ≈ 0.3 fA (with rate of 2 kHz) by reducing object and collimator slit openings [40].

The four SiC devices characterized during the experiment were mounted on a 30 × 30 mm^2 PCB board with a suitably sized opening of 15.2 × 15.2 mm^2 (see Fig. 2a). The board was attached to a mechanical actuator, allowing the positioning of the detector with submillimetric accuracy. A standard analog readout electronics was employed, composed of a 40 mV/MeV (Si) charge-sensitive preamplifier, placed inside the vacuum chamber, an ORTEC 572 Amplifier, and a Canberra ADC 8075 connected to the acquisition PC. The detector bias, ranging from −200 V to −1000 V, was supplied by an ORTEC 710 HV module. The SPECTOR software [41] was used for the DAQ. A similar electronics chain, based on ORTEC 142 A preamplifier and ORTEC 570 amplifier, was used for a passivated implanted planar silicon (PIPS) detector, which served for position calibration purposes.

Focused ions were raster-scanned over the SiC sensor using a calibrated electrostatic scanner that defined the ion positioning over millimeter-scale areas. The horizontal (x) and vertical (y) coordinates of each impinging proton were recorded together with the energy measured by the SiC detector, allowing to extract a 2D characterization of the device CCE. Different incident proton energies, provided by the two tandem accelerators available at RBI-AF, were used to perform the scanning, in order to probe the CCE also at different depths (z coordinate). A metal mesh of known pitch size (42 μm) was irradiated in supplementary runs to calibrate the scan size for each proton energy.

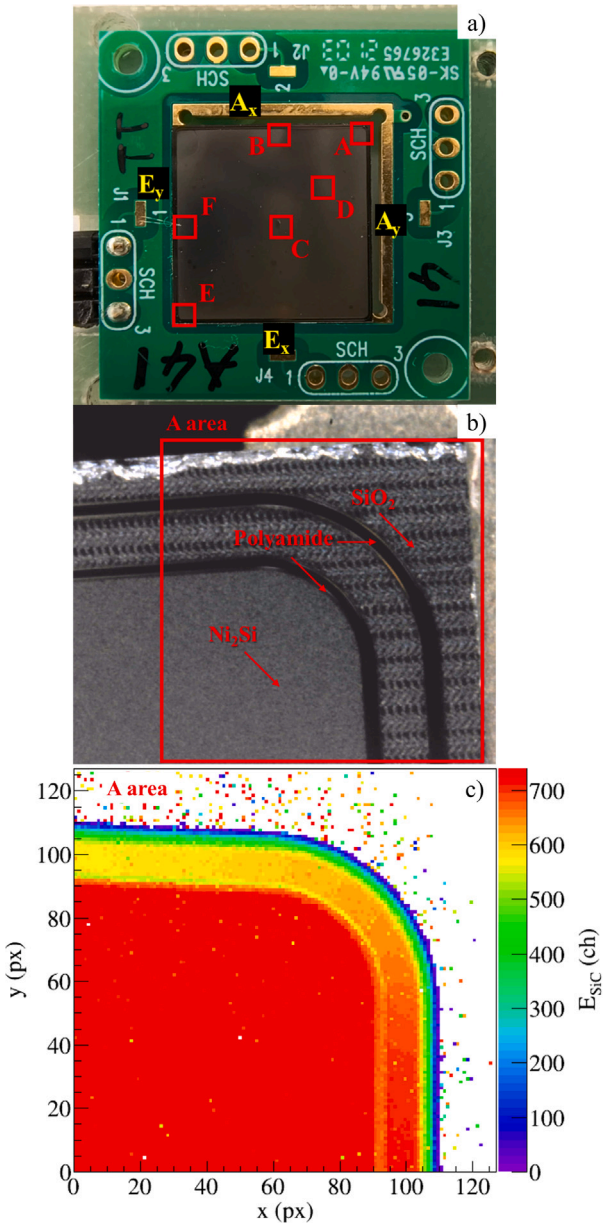

Fig. 2. Views of the TT0012-11 A41 SiC device. (a) Photo of the device mounted on the PCB board; A, B, C, D, E and F areas are indicated by the red boxes and the different edges explored are labeled as A_x, A_y, E_x, E_y. (b) microscopic view of the A area; materials visible from the top layer of the device are labeled in red; (c) IBIC 2D plot of the detector response at 3.40 MeV proton micro-beam incident energy on the A area.

The protons scattered by the mesh were detected by the PIPS detector of 300 μm thickness, placed at backward angles (*off-axis mode*).

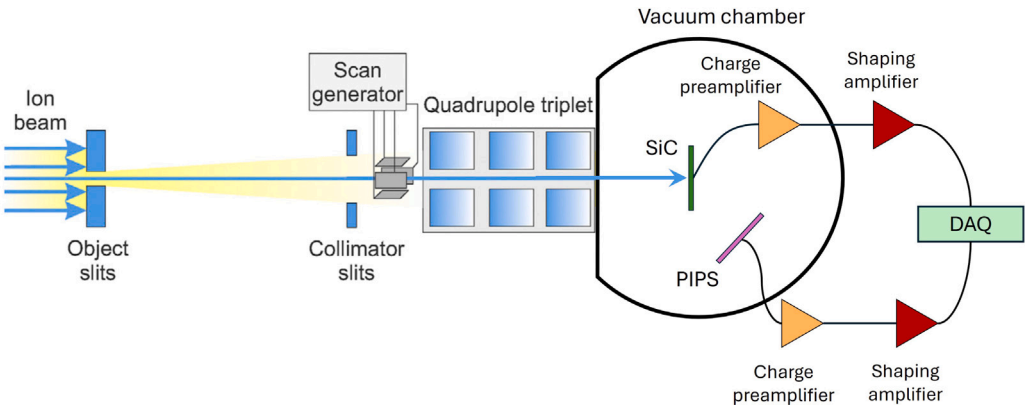

Fig. 3. Schematic view of the ion microprobe focusing and scanning system with IBIC pulse processing electronic chain. For the readout of the SiC and PIPS signals, charge sensitive preamplifiers and ORTEC 572 shaping amplifiers were used. Data acquisition was based on Canberra ADC 8075.

We performed a 3D characterization of the SiC CCE at five different bias voltages (full depletion voltage (FDV), FDV ± 15%, FDV ± 30%) and four different proton energies (1.26, 2.50, 3.40, 3.92 MeV) to study the SiC response at different depletion conditions and depths. The proton energies were chosen to explore a large range of detector depths, spanning from the near surface regions up to the full depletion depth, as shown by the proton ionization profiles in Fig. 4, which were deduced by the SRIM software [39]. The SiC detectors were irradiated on the front side in one inner area (active region, indicated as C in Fig. 2a) and two areas at the edge (indicated as A and E in Fig. 2a), thus exploring all the sides of the detectors, labeled as A_x, A_y, E_x, and E_y edges. Supplementary inner (D) and edge (B and F) areas were explored only in some configurations, as shown in Fig. 2a. In all cases, 128 × 128 pixels were used for imaging, choosing a total squared scan size of ≈ 1.3× 1.3 mm^2, corresponding to ≈ 10 × 10 μm^2 pixel size.

An example of a two-dimensional plot obtained from a scan of area A of the SiC sensor is shown in Fig. 2c. The horizontal and vertical axes represent the microbeam impact position in pixel coordinates, while the z-axis corresponds to the SiC detector response (E_{SiC}) in the same pixel, averaged over ≈ 10 events. This type of representation is commonly referred to as an IBIC 2D plot. The edge structure described in Section 2 and shown in Fig. 2b is clearly visible in the IBIC 2D plot of Fig. 2c. A fairly uniform response is observed in the inner region of the detector, followed by a decrease in the measured energy when crossing the first ring. The inner band between the two rings can then be identified, and finally, upon crossing the second ring, the detector response rapidly drops to zero.

4. 3D profiling of detector response

In order to characterize the detector response in the inner region and at the four edges, it is useful to study the CCE along the x- and y-directions of the explored areas. This could reveal differences in the borders and gives an estimation of the uniformity of the response in the active region. To this aim, the first step consists in the energy and position calibrations. From the full energy peak in the ADC channel spectra obtained for each proton bombarding energy, the response of the four SiC detectors was energy-calibrated. The extracted energy resolution of the SiC detectors ranges from 2% at 1.26 MeV to 0.7% at 3.92 MeV proton energies. While a detailed analysis of the resolution is beyond the scope of this paper, the observed trend can be attributed to multiple factors, mainly correlated to the number of generated electron–hole pairs, and electronic noise. Moreover, at lower proton energies, charge is deposited in a more localized volume (as visible in Fig. 4). This phenomenon can distort the internal electric field, and reduce the charge carrier drift velocity enhancing recombination effects. This leads to a decrease in the CCE and could possibly broader the signal.

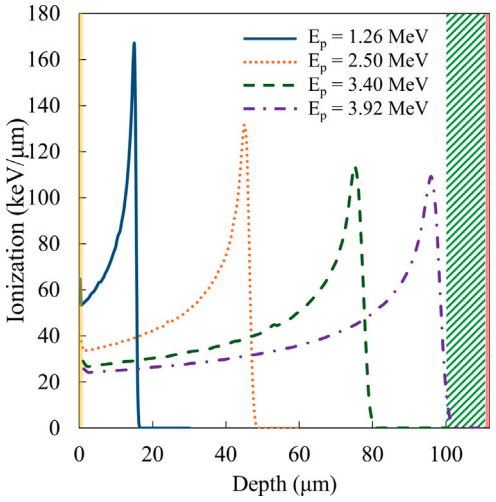

Fig. 4. Ionization profiles for the four proton energies used for the irradiation of SiC detectors, as obtained from simulations performed with the SRIM software [39]. Different materials are considered corresponding to the different layers of the SiC detector: Ni_2Si (yellow band), SiC (white band for the active region and green hatched band for the dead layer), and Al (red band).

Conversely, at higher energies, the Bragg peak becomes broader, and the carrier yield increases mitigating field distortion effects.

To perform the position calibration, the additional runs recorded in the same focusing conditions using the metal mesh were used. An example of the obtained 2D plot for 3.40 MeV protons measured by the PIPS detector is shown in Fig. 5. Each square visible in the plot is 42 × 42 μm^2 and allows to extract the pixel-to-meter conversion.

We defined the ratio E_{meas}/E_{beam}, where E_{meas} is the energy measured inside the detector and E_{beam} is the proton beam incident energy. It was extracted from the calibrated *2D IBIC plots* choosing a region of integration ≈ 200 μm wide over x, corresponding to the gray band shown in Fig. 6a, in which the E area is explored. The width of integration region comes from a compromise between keeping statistical uncertainty low and averaging over a region as small as possible. In the example shown in Fig. 6a, the E_{meas}/E_{beam} profile can be constructed along the y direction for the E_x border by the average of the detector response inside the gray band. The result is shown in Fig. 6b, in which the c axis is introduced as the distance from the physical edge of the SiC device. In this representation, the inner active area of the detectors starts at 400 μm and it is independent on the detector positioning into the mechanical support. In this way, it is possible to compare profiles belonging to different explored areas. We can see from Fig. 6b that

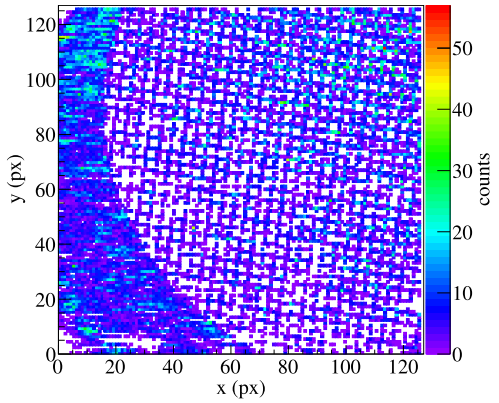

Fig. 5. 2D plot of the 3.40 MeV protons scattered by the 42 μm metal mesh and detected by the PIPS detector in off-axis mode.

the detector response is pretty constant inside the active region, then there is a drop of ≈ 10% of the signal crossing the first ring, because of the polyamide deposition and Al^{+} doped SiC layer that cause an energy loss to the crossing protons. Then, inside the band the signal goes again to ≈ 100%, as expected. Finally, after crossing the second ring, it drops rapidly to zero within ≈ 70 μm. However, looking at Fig. 6a, the detector response at the E_y edge appears to change along the *y* direction, suggesting a relevant difference between the two edges of this area. This aspect is further investigated later in this Section.

The CCE is defined as the ratio between E_{meas} and the fraction of E_{beam} released by the impinging protons in the active SiC volume. We neglected the energy loss in the thin Ni_2Si and SiO_2 layers, whereas the CCE was corrected for the not measurable energy loss in the thick layers present in the first guard ring. The obtained CCE is normalized to the inner region of the detector, where it is assumed to be 100%.

To quantify the uniformity of the SiC detectors response inside the active area, the CCE profiles, as a function of the horizontal coordinate c, in the C area were extracted and are shown in Fig. 7a and b for the TT0012-11 A41 and RA0089-27 A106 devices, respectively. Both devices are explored at the FDV and for different proton energies. Standard deviations of the distributions are smaller than 0.1% for both SiC detectors, with a slightly worse performance in the case of the RA0089-27 A106 SiC detector. We also note that the dispersion of the CCE exhibits a uniform distribution around the central value. Similar results are obtained for the other two SiC detectors under study. A comparable degree of uniformity was also observed in the exploration of area D and in the inner regions of areas A, B, E, and F. This observation suggests that the entire 1.5 × 1.5 cm^2 SiC surface exhibits consistent behavior. We can conclude that the CCE in the active region of the SiC detectors is pretty uniform and compliant with the NUMEN project requirements and more generally with their application in nuclear physics experiments.

To evaluate the detector response at its edges, it is interesting to study the CCE profiles as a function of the applied bias, as shown in Fig. 8. As the applied bias is increased the CCE profiles become sharper near the physical edges of the detector. Correspondingly, the SiC sensor active area increases, saturating around the FDV. Looking at the CCE curves measured at FDV-30%, we note a difference between devices belonging to the two wafers. In particular, we see a reduction of the CCE to ≈ 90% in the case of the RA0089-27 devices, explained by the stopping of the 3.40 MeV incident protons beyond the SiC active volume, since the depletion depth reached in this class of sensors is less than the nominal 100 μm [30].

A comparison between the CCE profiles measured on the four edges of the TT0012-11 A41 and RA0089-27 A106 devices is shown in Fig. 9a and b, respectively. It is clear that the detectors along their edge structure respond differently on the four sides, showing a reduction of

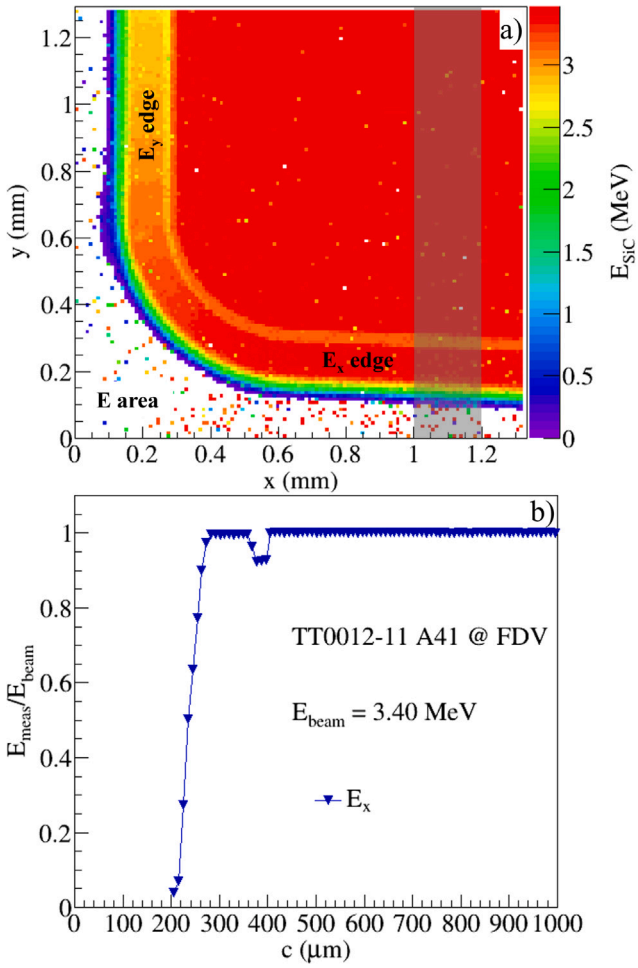

Fig. 6. IBIC measurement of the TT0012-11 A41 device at the FDV obtained by 3.40 MeV protons, in the E scanned area. (a) 2D scan of the 1.3 × 1.3 mm^2 E area. The gray band indicates the integration region of ≈ 200 μm width. (b) E_{meas}/E_{beam} profile extracted from the ROI indicated in panel (a), corresponding to the edge E_x (see Fig. 2a).

the CCE down to 80% around c ≈ 300 μm. A possible explanation of this phenomenon would be a non-uniformity of the SiO_2 layer covering the different edges (see Fig. 1) that corresponds to different energy losses by the incident protons. In this case, the observed signal reduction should correspond to a non-uniformity of several μm, which would be well above typical tolerances of epitaxial depositions. However, this hypothesis can be excluded looking at Fig. 10, in which the E_{meas}/E_{beam} profiles measured on the E_x and E_y edges at different incident proton energies are shown for the same SiC detectors of Fig. 9. Indeed, while in the region of the first ring, the energy loss increases as the proton incident energy decreases, in the region around 300 μm this effect is not present. This implies that the effect stems from a reduction of the efficiency in the collection of charges generated by the protons hitting the edges. In order to make a comparison between the four edges of each SiC detector, the CCE values extracted at ≈ 300 μm are listed in Table 1. We note that the reduction of CCE to ≈ 80% is systematically present in the A_x and E_y edges of each SiC sensor, whereas the other two edges show a CCE ≈ 100%, as expected. This phenomenon could arise from the cut of the wafers from which the SiC devices were produced (see Figure 2 in Ref. [8]), which systematically causes a failure in the electric field structure of the same borders in each sensor. Indeed, since SiC is a very hard material, the cutting process is not trivial. This analysis shows that, even when cutting with a grinding

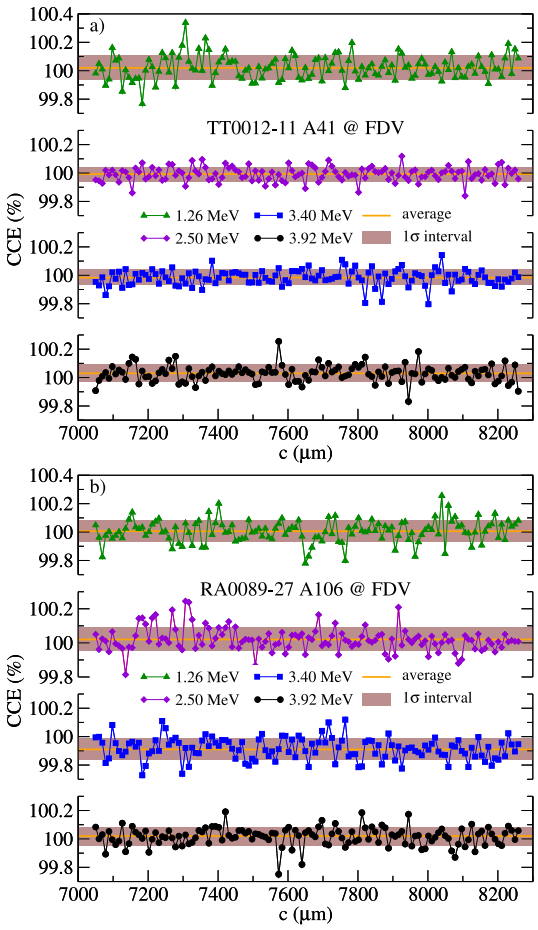

Fig. 7. CCE profiles measured on the TT0012-11 A41 (panel a) and RA0089-27 A106 (panel b) devices in the C area at different proton energies and at the FDV. The average CCE value and one standard deviation (σ) interval are indicated as the orange continuous line and the gray band, respectively.

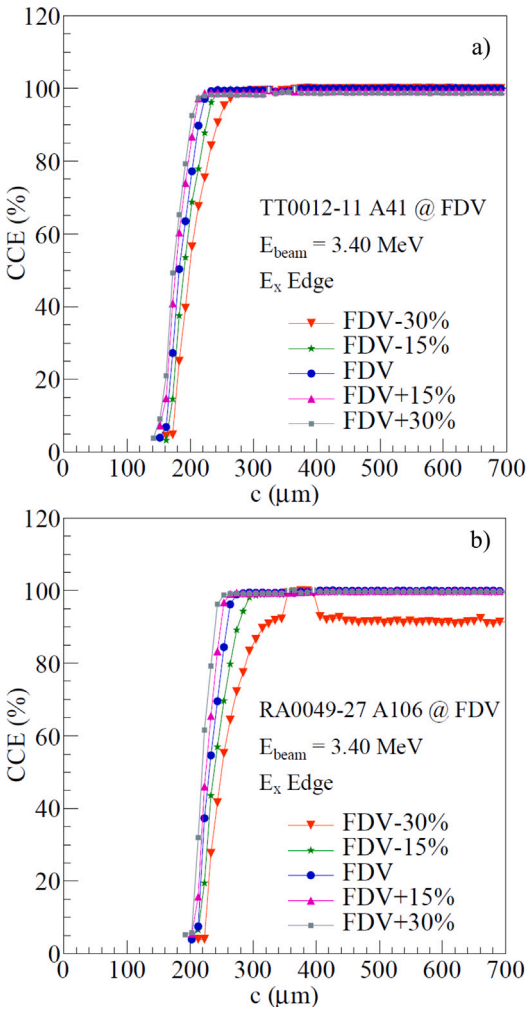

Fig. 8. Comparison between the CCE profiles measured at 3.40 MeV proton energy for the E_x edge and for different bias values of the TT0012-11 A41 (panel a) and RA0089-27 A106 (panel b) devices. In the region between the vertical lines, the CCE was corrected for the not measurable energy loss in the first guard ring.

wheel, there could be issues in one of the cut edge, and thus further development of the processing technique is still necessary.

5. Conclusions

State-of-the-art large area SiC detectors were characterized in order to verify their performances in terms of the NUMEN project requirements and more in general in application in nuclear physics experiments. Sensors were produced from two different wafers (TT0012-11 and RA0089-27), displaying different FDV, doping profiles, and depletion depths [8,30].

In order to guide further R&D activities on SiC sensors, investigations on the charge collection efficiency behavior in the full active volume and near the edges of the detectors with micrometer precision were conducted for the first time and presented in this work. This was done using the ion beam-induced charge technique with focused MeV range protons with beam spot ≈ 2 μm and ≈ 10 × 10 μm^2 pixel size. Different areas of the SiC sensors were explored with different proton incident energies, in order to explore the 3D detector response. Also, the dependence on the applied bias was studied by five different values around the FDV. The CCE profiles along the horizontal and vertical coordinates were built, averaging inside 200 μm wide regions. Differently from what found in other kind of characterizations [8,30], SiC belonging to the two wafers do not display significant differences in terms of the CCE behavior, both in the inner area and at the edges.

The CCE in the inner active area of the SiC detectors is pretty uniform and displays standard deviations smaller than 0.1% with a uniform distribution around the central value. This result is encouraging for the application of SiC detectors in nuclear physics experiments and, in particular, it confirms that the present SiC sensors are compliant with the NUMEN project requirements.

Concerning the edge areas, starting from the physical edge, we observed in two edges (A_y and E_x) that in the first 200 μm CCE = 0 and, after this region, it shows a sharp increase up to 100% within ≈ 70 μm. In the region 250 ÷ 350 μm, the CCE is ≈ 100% then, where a first guard ring (≈ 30 μm wide) is crossed, there is a drop in the measured energy due to a different energy loss in a thick layer of polyamide (≈ 8 μm) and Al^+ doped SiC (≈ 5 μm). After crossing this region, the internal active area starts, where CCE is assumed to be 100%. The CCE profile thus obtained will be used as input of advanced simulations with GEANT4-based tools to evaluate both the overall detection efficiency and the cross-section sensitivity of the future PID system of the MAGNEX spectrometer.

A different behavior is observed in the other two edges (A_x and E_y), in which a drop of the CCE down to ≈ 80% is found in the region 250 ÷ 350 μm. This behavior, common to all the irradiated devices and independent on the wafer, could cause a degradation in the overall

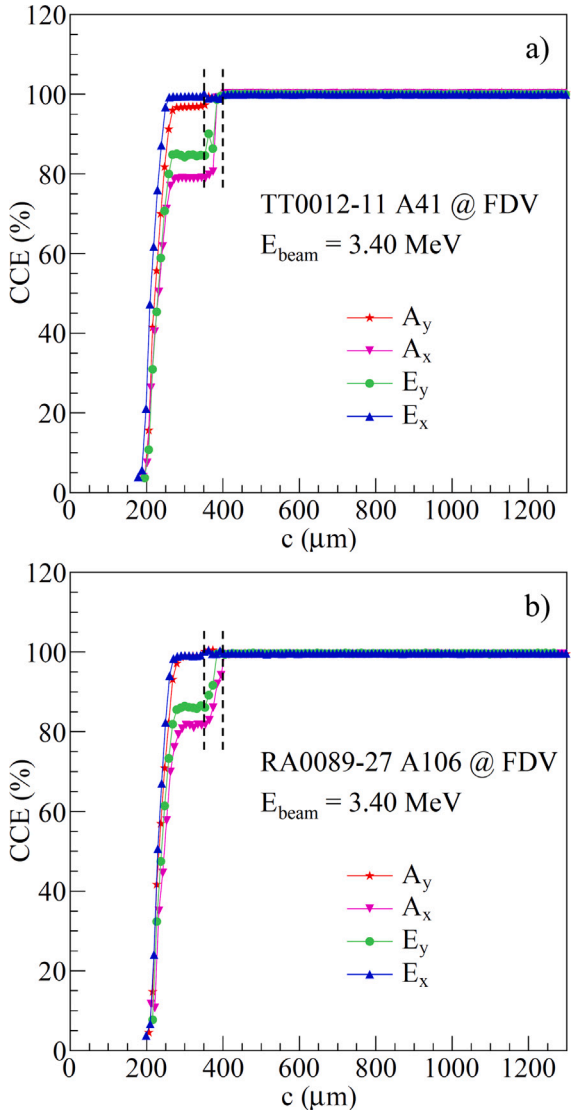

Fig. 9. Comparison between the CCE profiles measured at 3.40 MeV proton energy on the four edges of the TT0012-11 A41 (panel a) and RA0089-27 A106 (panel b) devices at the FDV. In the region between the vertical lines, the CCE was corrected for the not measurable energy loss in the first guard ring.

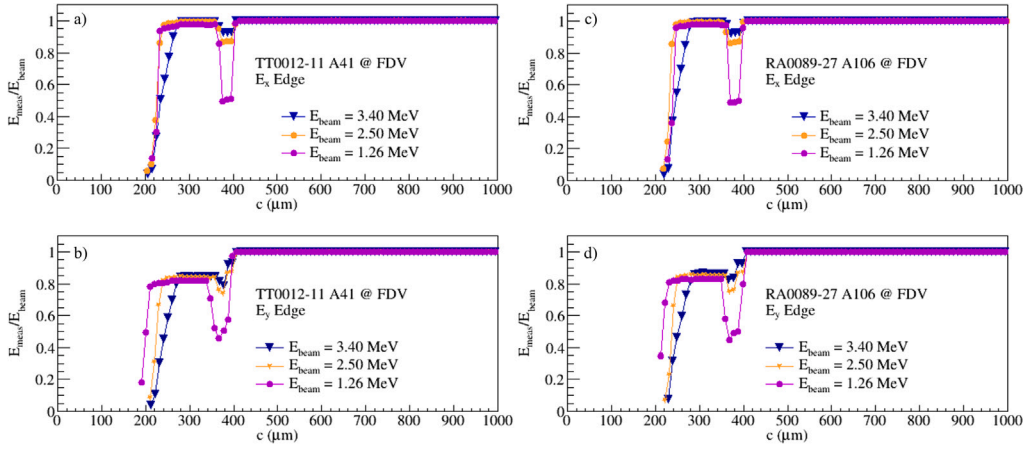

Fig. 10. Comparison between the E_{meas}/E_{beam} profiles for the E_x and E_y edges at the FDV measured for different proton incident energies for the TT0012-11 A41 and RA0089-27 A106 devices.

energy resolution and tricky problems in the use of such detectors for particle identification purposes [42]. The systematic observation of this phenomenon on specific edges, suggests a problem arising from the cut done on the wafers to separate the produced SiC devices. Guided from the results of this paper, a new production of SiC detectors was recently started with further improvements on the cutting techniques (e.g. grinding wheel) and widening of the edge structure. They will be tested through the techniques reported in this paper, once the detector production is accomplished.

CRediT authorship contribution statement

A. Spatafora: Writing – original draft, Supervision, Software, Methodology, Investigation, Formal analysis, Data curation, Conceptualization. **D. Carbone:** Writing – review & editing, Writing – original draft, Validation, Supervision, Project administration, Methodology, Investigation, Funding acquisition, Formal analysis, Data curation, Conceptualization. **L. La Fauci:** Writing – review & editing, Software, Formal analysis, Data curation. **G.A. Brischetto:** Writing – review & editing, Methodology, Investigation, Formal analysis, Data curation, Conceptualization. **D. Calvo:** Writing – review & editing, Methodology, Formal analysis, Data curation. **F. Cappuzzello:** Writing – review & editing, Supervision, Methodology, Formal analysis, Data curation, Conceptualization. **M. Cavallaro:** Writing – review & editing, Supervision, Methodology, Formal analysis, Data curation, Conceptualization. **A. Crnjac:** Software, Methodology, Investigation. **K. Ivanković Nizić:** Software, Methodology, Investigation. **M. Jakšić:** Software, Methodology, Investigation, Conceptualization. **D. Torresi:** Methodology, Investigation. **S. Tudisco:** Methodology, Conceptualization.

Declaration of competing interest

The authors declare the following financial interests/personal relationships which may be considered as potential competing interests: Alessandro Spatafora reports financial support was provided by EuroLABS. Alessandro Spatafora reports financial support was provided by Next generation EU. Diana Carbone reports financial support was provided by EuroLABS. Diana Carbone reports financial support was provided by Next Generation EU. Laura La Fauci reports financial support was provided by Next generation EU. If there are other authors, they declare that they have no known competing financial interests or personal relationships that could have appeared to influence the work reported in this paper.

Acknowledgments

The authors acknowledge the financial support for transnational access to the RBI accelerator facility by the project EURO-Labs funded from the European Union's Horizon Europe Research and Innovation programme under Grant Agreement No. 101057511. This project received funding from the European Union "Next Generation EU" (PNRR M4 - C2 – Inv. 1.1 - DD n. 104 del 02-02-2022 - PRIN 20227Z4HB8).

Data availability

Data will be made available on request.

References

[1] M. He, et al., Investigation of the synergistic effects on 4H-SiC junction barrier schottky diodes after multiple irradiation, Nucl. Instrum. Methods Phys. Res. Sect. B: Beam Interactions Mater. Atoms 549 (2024) 165288, http://dx.doi.org/10.1016/j.nimb.2024.165288.

[2] C. Altana, et al., Radiation damage by heavy ions in silicon and silicon carbide detectors, Sensors 23 (14) (2023) http://dx.doi.org/10.3390/s23146522.

[3] C. Ciampi, et al., Nuclear fragment identification with ΔE-E telescopes exploiting silicon carbide detectors, Nucl. Instrum. Methods Phys. Res. Sect. A: Accel. Spectrometers, Detect. Assoc. Equip. 925 (2019) 60–69, http://dx.doi.org/10.1016/j.nima.2019.01.085.

[4] G. Raciti, M. De Napoli, F. Giacoppo, E. Rapisarda, C. Sfienti, Detection properties and radiation damage effects in SiC diodes irradiated with light ions, Nucl. Phys. A 834 (1) (2010) 784c–787c, http://dx.doi.org/10.1016/j.nuclphysa.2010.01.146.

[5] F. Ruddy, et al., The fast neutron response of 4H silicon carbide semiconductor radiation detectors, IEEE Trans. Nucl. Sci. 53 (3) (2006) 1666–1670, http://dx.doi.org/10.1109/TNS.2006.875151.

[6] X. Zhang, et al., Characterizing the timing performance of a fast 4H-SiC detector with an ^{241}Am source, IEEE Trans. Nucl. Sci. 60 (2013) 2352–2356.

[7] S. Tudisco, et al., SiCilia-silicon carbide detectors for intense luminosity investigations and applications, Sensors 18 (7) (2018) http://dx.doi.org/10.3390/s18072289.

[8] D. Carbone, et al., Characterization of newly developed large area SiC sensors for the NUMEN experiment, Nucl. Instrum. Methods Phys. Res. Sect. A: Accel. Spectrometers, Detect. Assoc. Equip. 1069 (2024) 169960, http://dx.doi.org/10.1016/j.nima.2024.169960.

[9] Samothrace project, Sicilian Micro and Nano Technology Research and Innovation Center, 2024, URL https://samothrace.eu/.

[10] D. Carbone, et al., Prototyping of a high resolution, radiation hard, and portable SiC-csi particle identification system for heavy-ion nuclear reactions, 2022, PRIN 20227Z4HB8 founded by European Union "Next Generation EU".

[11] F. Cappuzzello, et al., The NUMEN project: Nuclear matrix elements for neutrinoless double beta decay, Eur. Phys. J. A 54 (2018) 72, http://dx.doi.org/10.1140/epja/i2018-12509-3.

[12] F. Cappuzzello, et al., The NUMEN technical design report, Internat. J. Modern Phys. A 36 (2021) 2130018, http://dx.doi.org/10.1142/S0217751X21300180.

[13] Spectrometric performance of SiC radiation detectors at high temperature, Radiat. Phys. Chem. 214 (2024) 111283, http://dx.doi.org/10.1016/j.radphyschem.2023.111283.

[14] M. Agostini, G. Benato, J.A. Detwiler, J. Menéndez, F. Vissani, Toward the discovery of matter creation with neutrinoless $\beta\beta$ decay, Rev. Modern Phys. 95 (2023) 025002, http://dx.doi.org/10.1103/RevModPhys.95.025002.

[15] F. Cappuzzello, et al., Shedding light on nuclear aspects of neutrinoless double beta decay by heavy-ion double charge exchange reactions, Prog. Part. Nucl. Phys. 128 (2023) 103999, http://dx.doi.org/10.1016/j.ppnp.2022.103999.

[16] F. Cappuzzello, C. Agodi, D. Carbone, M. Cavallaro, The MAGNEX spectrometer: results and perspectives, Eur. Phys. J. A52 (6) (2016) 167, http://dx.doi.org/10.1140/epja/i2016-16167-1, arXiv:1606.06731.

[17] M. Cavallaro, et al., The MAGNEX magnetic spectrometer for double charge exchange reactions, Nucl. Instrum. Methods Phys. Res. Sect. B: Beam Interactions Mater. Atoms 463 (2020) 334–338, http://dx.doi.org/10.1016/j.nimb.2019.04.069.

[18] V. Soukeras, et al., Measurement of the double charge exchange reaction for the^{20}Ne +^{130}Te system at 306 MeV, Results Phys. 28 (2021) 104691, http://dx.doi.org/10.1016/j.rinp.2021.104691.

[19] C. Eke, et al., Measurement of the^{116}Sn(^{18}O,^{18}Ne)^{116}Cd double charge exchange reaction at 276 MeV, Results Phys. 67 (2024) 108037, http://dx.doi.org/10.1016/j.rinp.2024.108037.

[20] E.M. Gandolfo, et al., Response of G-NUMEN LaBr3(Ce) detectors to high counting rates, Instruments 7 (3) (2023) http://dx.doi.org/10.3390/instruments7030028.

[21] I. Ciraldo, et al., Characterization of a gas detector prototype based on thick-GEM for the MAGNEX focal plane detector, Nucl. Instrum. Methods Phys. Res. Sect. A: Accel. Spectrometers, Detect. Assoc. Equip. 1048 (2023) 167893, http://dx.doi.org/10.1016/j.nima.2022.167893.

[22] D. Calvo, et al., Present outcome from the NUMEN R&D phase, Nucl. Instrum. Methods Phys. Res. Sect. A: Accel. Spectrometers, Detect. Assoc. Equip. 1041 (2022) 167336, http://dx.doi.org/10.1016/j.nima.2022.167336.

[23] C. Agodi, et al., The NUMEN project: toward new experiments with high-intensity beams, Universe 7 (72) (2021) http://dx.doi.org/10.3390/universe7030072.

[24] P. Finocchiaro, et al., The NUMEN heavy ion multidetector for a complementary approach to the neutrinoless double beta decay, Universe 6 (9) (2020) http://dx.doi.org/10.3390/universe6090129.

[25] F. Iazzi, et al., A new cooling technique for targets operating under very intense beams, WIT Trans. Eng. Sci. 116 (2017) 61–70.

[26] F. Cappuzzello, M. Cavallaro, A. Cunsolo, A. Foti, D. Carbone, S. Orrigo, M. Rodrigues, A particle identification technique for large acceptance spectrometers, Nucl. Instrum. Methods Phys. Res. Sect. A: Accel. Spectrometers, Detect. Assoc. Equip. 621 (1) (2010) 419–423, http://dx.doi.org/10.1016/j.nima.2010.05.027.

[27] G. Knoll, Radiation Detection and Measurement, Wiley, 2010.

[28] S. Agostinelli, et al., Geant4-a simulation toolkit, Nucl. Instrum. Methods Phys. Res. Sect. A: Accel. Spectrometers, Detect. Assoc. Equip. 506 (3) (2003) 250–303, http://dx.doi.org/10.1016/S0168-9002(03)01368-8.

[29] J. Allison, et al., Recent developments in Geant4, Nucl. Instrum. Methods Phys. Res. Sect. A: Accel. Spectrometers, Detect. Assoc. Equip. 835 (2016) 186–225, http://dx.doi.org/10.1016/j.nima.2016.06.125.

[30] A. Spatafora, et al., Depletion depth measurements of new large area silicon carbide detectors, Nucl. Instrum. Methods Phys. Res. Sect. A: Accel. Spectrometers, Detect. Assoc. Equip. 1080 (2025) 170670, http://dx.doi.org/10.1016/j.nima.2025.170670.

[31] M. Jakšić, et al., Ion microbeam studies of charge transport in semiconductor radiation detectors with three-dimensional structures: an example of LGAD, Front. Phys. 10 (2022) http://dx.doi.org/10.3389/fphy.2022.877577.

[32] M. Pezzarossa, et al., Polychromatic angle resolved IBIC analysis of silicon power diodes, Nucl. Instrum. Methods Phys. Res. Sect. B: Beam Interactions Mater. Atoms 488 (2021) 50–63, http://dx.doi.org/10.1016/j.nimb.2020.12.006.

[33] J. Garcia Lopez, et al., Comparative study by IBIC of si and SiC diodes irradiated with high energy protons, Nucl. Instrum. Methods Phys. Res. Sect. B: Beam Interactions Mater. Atoms 372 (2016) 143–150, http://dx.doi.org/10.1016/j.nimb.2015.12.029.

[34] A. Lo Giudice, Y. Garino, C. Manfredotti, V. Rigato, E. Vittone, Angle resolved IBIC analysis of 4H-SiC schottky diodes, Nucl. Instrum. Methods Phys. Res. Sect. B: Beam Interactions Mater. Atoms 249 (1) (2006) 213–216, http://dx.doi.org/10.1016/j.nimb.2006.03.168.

[35] C. Yang, et al., Ion-beam-induced-charge characterisation of particle detectors, Nucl. Instrum. Methods Phys. Res. Sect. B: Beam Interactions Mater. Atoms 190 (1) (2002) 212–216, http://dx.doi.org/10.1016/S0168-583X(02)00456-1.

[36] M. Jiménez-Ramos, et al., IBIC analysis of SiC detectors developed for fusion applications, Radiat. Phys. Chem. 177 (2020) 109100, http://dx.doi.org/10.1016/j.radphyschem.2020.109100.

[37] S. Tudisco, et al., Silicon carbide devices for radiation detection: A review of the main performances, Nucl. Instrum. Methods Phys. Res. Sect. A: Accel. Spectrometers, Detect. Assoc. Equip. 1072 (2025) 170112, http://dx.doi.org/10.1016/j.nima.2024.170112.

[38] J.F. Ziegler, J.P. Biersack, The stopping and range of ions in matter, in: D.A. Bromley (Ed.), Treatise on Heavy-Ion Science: Volume 6: Astrophysics, Chemistry, and Condensed Matter, Springer US, Boston, MA, 1985, http://dx.doi.org/10.1007/978-1-4615-8103-1_3.

[39] J.F. Ziegler, M. Ziegler, J. Biersack, SRIM-the stopping and range of ions in matter, Nucl. Instrum. Methods Phys. Res. Sect. B: Beam Interactions Mater. Atoms 268 (11) (2010) 1818–1823, http://dx.doi.org/10.1016/j.nimb.2010.02.091.

[40] C. Jeynes, R.P. Webb, A. Lohstroh, Ion beam analysis: A century of exploiting the electronic and nuclear structure of the atom for materials characterisation, Rev. Accel. Sci. Technol. 04 (01) (2011) 41–82, http://dx.doi.org/10.1142/S1793626811000483.

[41] D. Cosic, M. Bogovac, M. Jakšić, Data acquisition and control system for an evolving nuclear microprobe, Nucl. Instrum. Methods Phys. Res. Sect. B: Beam Interactions Mater. Atoms 451 (2019) 122–126, http://dx.doi.org/10.1016/j.nimb.2019.05.047.

[42] C. Lombardo, et al., Design and performance of the prototype of the new particle identification system for the MAGNEX spectrometer within the NUMEN project, J. Instrum. 20 (06) (2025) C06053, http://dx.doi.org/10.1088/1748-0221/20/06/C06053.